IEEE Photonics Journal
An IEEE Photonics Society Publication

Open Access

Multiple Extraordinary Optical Transmission Peaks via a Single Subwavelength Slit Surrounded by Mixed-Period Grooves

Volume 5, Number 5, October 2013

Ying-jie Su
Hung-chun Chang, Senior Member, IEEE

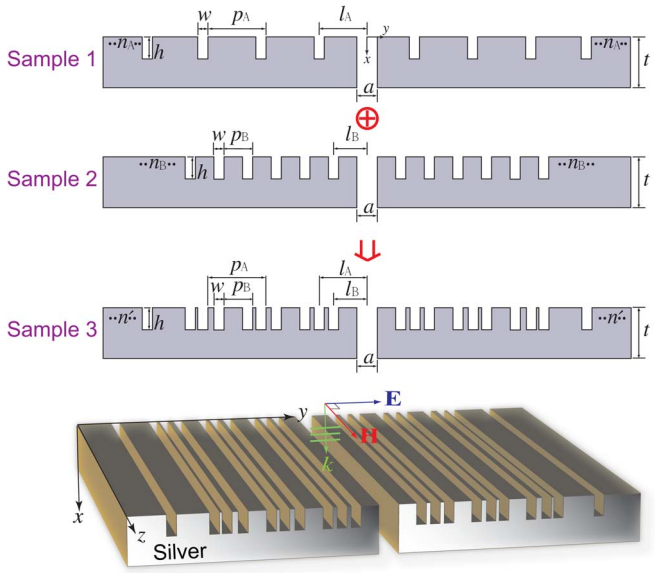

DOI: 10.1109/JPHOT.2013.2281980
1943-0655

Multiple Extraordinary Optical Transmission Peaks via a Single Subwavelength Slit Surrounded by Mixed-Period Grooves

Ying-jie Su[1] **and Hung-chun Chang,**[1,2] ***Senior Member, IEEE***

[1]Graduate Institute of Photonics and Optoelectronics, National Taiwan University, Taipei 10617, Taiwan
[2]Graduate Institute of Communication Engineering and the Department of Electrical Engineering, National Taiwan University, Taipei 10617, Taiwan

DOI: 10.1109/JPHOT.2013.2281980

Manuscript received August 7, 2013; revised September 1, 2013; accepted September 4, 2013. Date of publication September 16, 2013; date of current version September 27, 2013. This work was supported in part by the National Science Council of the Republic of China under Grants NSC 100-2221-E-002-182-MY2 and NSC 101-2221-E-002-147-MY2, by the Excellent Research Projects of National Taiwan University under Grant 102R89081, and by the Ministry of Education of the Republic of China under "The Aim of Top University Plan" grant. Corresponding author: H.-C. Chang (e-mail: hcchang@cc.ee.ntu.edu.tw).

Abstract: In this paper, we use mixed-period grooves to surround a subwavelength slit to realize multiple extraordinary transmittance peaks for transmitted light. The mixed-period grooves refer to a set of 1-D grooves arranged with particular groove pitches, which are formed by merging two sets of 1-D periodic grooves with similar geometries but mainly different groove periodicities. The finite-difference time-domain method was used to calculate the transmittance spectra for the proposed mixed-period slit-groove structure over the visible regime. The calculated spectra show that the mixed-period grooves could induce dual groove-generated extraordinary transmission peaks in the visible regime. We find that the mixed-period grooves can act as a grating coupler to excite surface plasmon polaritons at multiple incident wavelengths. Moreover, one approach has been presented to further boost the transmission at the dual groove-generated peaks.

Index Terms: Aperture transmission, gratings, subwavelength structures, surface plasmons.

1. Introduction

In general, lightwave had been considered difficult to pass through a subwavelength aperture [1] (that is, low transmittance); the term subwavelength means the aperture size is smaller than the light wavelength. The aforementioned constraint for light thus became a substantial limitation to the applications of photonic devices at nano-scale dimensions, like the size-compatibility problem [2] for photonics and electronics. However, in 1998, the extraordinary optical transmission (EOT; that is, high transmittance) was first discovered [3] for light passing through subwavelength metal holes. From then on, vast theoretical and experimental studies have been performed in understanding the interaction of light with metals in various nano-structures, such as a single subwavelength aperture [4], [5] and subwavelength aperture arrays [6]–[8]. The EOT draws great attention because it has vast potential for applications in many fields [9], including photolithography [10], [11], optical data storage [10], [12], organic light-emitting diodes [13], and photodetectors [14]–[17].

Among the aforementioned applications, the one for photodectors is to use the EOT of bull's-eye (BE) structures to boost light transmittance [14]–[17]. Such structures are a kind of plasmonic nano-structures, which consist of a single metal aperture surrounded with periodic surface corrugations,

for example, a single hole surrounded by concentric annular grooves (also termed the 2-D BE structure) and/or a single slit surrounded by parallel linear grooves (also termed the 1-D BE structure). The 1-D BE structure is called the single-period slit-groove (SPSG) structure in later sections, because surrounding grooves of the BE structure are arranged with a single groove periodicity. In fact, experimental results of the EOT phenomena for the 1-D and 2-D BE structures were reported in [18] and [19]; since then, much work [20]–[25] has focused on the transmission properties of these BE structures. Recently, some groups [26]–[31] explored the underlying mechanisms of the EOT for these BE structures, and some others [32]–[35] optimized the geometrical parameters for enhancing the EOT for these BE structures. In addition, the BE-structure-related applications [10], [14]–[17] have also been proposed.

So far, it is generally recognized that the mechanism for the groove-generated EOT for these BE structures is due to the excitation of surface plasmon polaritons (SPPs) [18], [20], [22], [23], [26], [29], [30], [36], [37]. The SPPs come from the coupling between free surface charges of the metal and the incident light, where the momentum mismatch between the SPPs and the incident light is compensated via the periodicities of the surface grooves of the BE structures. To be specific, the periodic surface grooves act like an antenna to couple the incident light into SPPs, which make the electromagnetic (EM) field become intense above the single aperture, leading to the EOT peak [9]. Here, the wavelength of the EOT peak is mainly determined by the period of the surrounding grooves [18], [22], [26]. Recently, the slit-to-groove distance (a geometry parameter of the BE structure) has been considered [22], [31], [35], [38], [39] as a key parameter to boost the transmittance of the groove-generated EOT peak of the BE structure. Afterwards, a microscopic theory for the 1-D BE structure has been provided to support that the occurrence of the groove-generated EOT peak is due to the constructive interference between the slit modes (due to the Fabry-Pérot (F-P) like resonance of the subwavelength slit) that are excited by the incident light and by the groove-generated SPPs [29].

However, most BE-structure-related works have focused on using periodic surface corrugations to surround a subwavelength aperture; for example, the surrounding groove pitches of the mentioned 1-D BE or SPSG structure are arranged with a single periodicity. On the other hand, the number of the available groove-generated EOT peaks in the visible regime is limited to one for such SPSG structure. This limitation would limit the BE structure to applications which need to be operated at multiple working wavelengths within the visible regime, such as dual-wavelength optical filters. Also, little literature has reported how to use non-periodic surface corrugations to effectively generate the groove-generated EOT peaks for a subwavelength aperture. For these reasons, this study designs the mixed-period grooves and uses them to surround the subwavelength slit to achieve multiple groove-generated EOT peaks for the transmitted light. Unlike the mentioned periodic grooves which show a constant regular groove pitch, the proposed mixed-period grooves display carefully designed irregular groove pitches.

In this study, we use the 1-D mixed-period grooves to surround a subwavelength slit to form the mixed-period slit-groove (MPSG) structure, i.e., Sample 3 in Fig. 1, for realizing multiple groove-generated EOT peaks at arbitrary wavelengths in the visible regime, for the transmitted light. Here, the MPSG structure is formed by combining two SPSG structures, i.e., Samples 1 and 2 in Fig. 1. The rest of this paper is outlined as follows. We first confirm the spectral features of Samples 1 and 2. Next, we turn to explore the spectral features of Sample 3. Then, a comparison of transmittance spectra for groove-generated peaks is made between Sample 3 and Samples 1 and 2. Furthermore, the underlying mechanism of the EOT for Sample 3 is investigated. Finally, one way is presented to boost the transmittance for the multiple groove-generated EOT peaks. Note that for all the samples, this work has concentrated mainly on the groove-generated EOT peaks launched by the grooves, instead of the F-P like EOT peaks launched by the subwavelength slit.

2. Simulation Setup and Modeled Structures

This section describes the modeled structures, the numerical scheme, and related parameters for our numerical simulations. Samples 1 and 2 are combined to form the proposed structure, Sample 3,

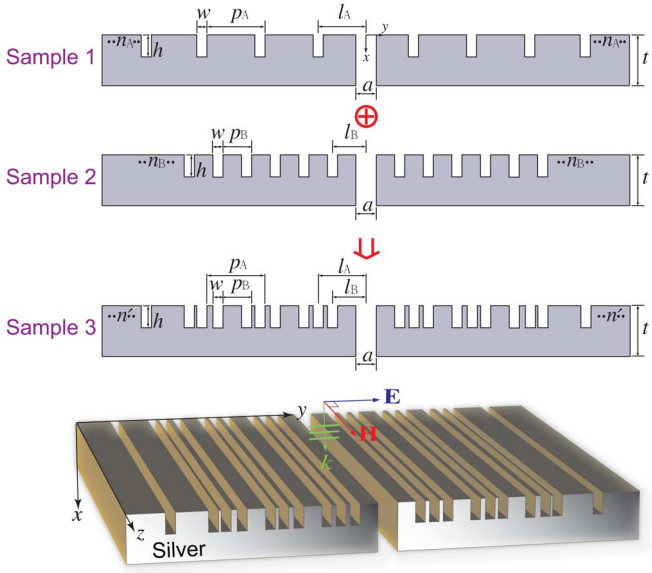

Fig. 1. Schematics of two SPSG structures (Samples 1 and 2) and the proposed MPSG structure (Sample 3). Sample 3 is obtained by combining Samples 1 and 2. For Samples 1 and 2, the surrounding grooves are periodic, with groove pitch (or period), groove number, and slit-to-groove distance denoted, respectively, by p_A, $2n_A$, l_A and p_B, $2n_B$, l_B. For Sample 3, the surrounding grooves are non-periodic, with groove pitches, groove number, and slit-to-groove distances denoted, respectively, by $(p_A; p_B)$, $2n'$ [here $n' \equiv (n_A; n_B)$], and l_A and l_B. All these samples have the same groove width w, groove height h, slit width a, and film thickness t. All structures are assumed to be infinite in the z direction. The lowest diagram shows an oblique view for Sample 3.

in this study. Each sample is composed of a finite number of grooves surrounding a single subwavelength slit. By aligning their central slits, Samples 1 and 2 are merged to form Sample 3. After the merging process, the resultant grooves of Sample 3 show irregular groove pitches surrounding the single slit, because Samples 1 and 2 have different groove periods.

Geometrical parameters of Samples 1, 2, and 3 are shown in Fig. 1. The slit-to-groove distance is defined as the distance from the center of the first groove, which is closest to the slit, to the center of the slit for an SPSG structure. In this work, the grooves surrounding the slit are with the groove period, groove number, and the slit-to-groove distance respectively being $p_A = 730$ nm, $2n_A$, and $l_A = 730$ nm for Sample 1 and $p_B = 600$ nm, $2n_B$, and $l_B = 600$ nm for Sample 2. Here, the parameter n_A and/or n_B are varied from 2 to 8 for observing the influence of the groove number on the transmittance. For Sample 3, its geometrical features such as groove pitches are mainly determined by p_A and l_A of Sample 1 and p_B and l_B of Sample 2. Note that for Sample 3, the resultant number of the mixed-period grooves $(2n')$ is equal to $2n_A + 2n_B$, since Sample 3 is formed by combining Sample 1 with the groove number $2n_A$ and Sample 2 with the groove number $2n_B$. Also, note that for convenience, n' is expressed by $(n_A; n_B)$ hereafter. We consider that Samples 1, 2, and 3 are all made of silver and have the same groove width $w = 40$ nm, groove height $h = 90$ nm, slit width $a = 40$ nm, and film thickness $t = 350$ nm. The aforementioned geometrical parameters are selected because they are close to typical values in experiments in the visible regime [26].

For calculating the transmittance spectra for these three samples, a plane wave with a sine-modulated Gaussian waveform is impinged normally on the corrugated surface of each sample from above. The central wavelength is $\lambda_c = 630$ nm since this work has focused on the optical regime, i.e., the free-space wavelength range is from 400 nm to 860 nm. All the spectra have been calculated with a step size of 2 nm in wavelength in this study. And the transverse-magnetic (TM) wave (i.e., $E_z = H_x = H_y = 0$) is used to excite the SPPs on the interface between air and the metal film.

Owing to the irregular geometry such as the non-periodic groove pitches of Sample 3, the numerical finite-difference time-domain (FDTD) approach [40] was used in this study for solving the

time dependent Maxwell's equation for the EM fields for Sample 3. In order to simulate the extension of the free space to infinity, perfectly matched layers (PMLs) [40] were put on boundaries to surround the computational domain along the x and y directions. The cell number over the PML thickness was set to 20. Also, an auxiliary differential equation method [40] was used to combine Maxwell's equations with the dispersion relation for modeling dispersive property of silver. The dispersive property was approximated by the Drude model. According to the Drude model, the relative permittivity (in frequency domain) of a real metal is given by

$$\epsilon_m(\omega) = \epsilon_\infty - \frac{\omega_p^2}{\omega^2 + i\gamma\omega}. \tag{1}$$

In (1), ω is the angular frequency of the impinging light, ϵ_∞ is the relative permittivity at infinite frequency in the metal, ω_p is the plasma frequency in the metal, and γ is the damping constant in the metal. This study chooses $\epsilon_\infty = 5$, $\omega_p = 1.37 \times 10^{16}$ s^{-1}, and $\gamma = 9.63 \times 10^{13}$ s^{-1} as a set of parameters to fit the experimental relative permittivity data [41] for silver over the visible regime. The computational domain (does not include the PMLs) was set to 1.76-μm width in the x direction ($-0.8\ \mu\text{m} \le x \le 0.96\ \mu\text{m}$ in Fig. 1) and 15.39-μm width in the y direction ($0\ \mu\text{m} \le y \le 15.39\ \mu\text{m}$ in Fig. 1) for simulating each sample in Fig. 1. The grid size was set to $\Delta x = \Delta y = 2.5$ nm along the x and y directions. In addition, the discrete Fourier transform was used to convert the time-domain results (EM fields) into the complex phasor form to calculate the transmittance spectra.

The normalized transmittance T is denoted by the ration of the transmitted power flux and the impinging power flux. In this study, the transmittance is normalized to the cross-sectional area of the slit. The normalized transmittance T is defined as following:

$$T = \frac{\left[\int_{A_{out}} (P_x)\, dA_{out}\right] \Big/ A_{out}}{\left[\int_{A_{in}} (P_x)\, dA_{in}\right] \Big/ A_{in}} = \frac{PA_{in}}{P_0 A_{out}}. \tag{2}$$

In (2), P_x is the x component of the Poynting vector over the slit exit, P is the power flux passing through the slit by integrating P_x over the exit surface of the slit, and P_0 is the power flux passing through a virtual slit (by integrating P_x over the entrance surface of the virtual slit). Here, the virtual slit means a null slit (i.e., without the metal film) in the free space. A_{out} is the cross-sectional area of the exit surface of the slit, and A_{in} is the cross-sectional area of the entrance surface of the virtual slit. In addition, we have confirmed the validity of our simulation program by comparing our result with the transmittance spectrum calculated in [26] using the coupled-mode method for simulating the same typical slit-groove structure.

3. Results and Discussion

Before exploring the EOT for the MPSG structure (Sample 3), we first examine the EOT for the two SPSG structures (Samples 1 and 2) with those geometrical parameters as stated in Section 2. Since Sample 3 is formed by combining Samples 1 and 2, in this section, the transmission spectra for Samples 1 and 2 will be shown first.

3.1. Single Groove-Generated EOT Peaks of Samples 1 and 2

In Fig. 2, a single groove-generated peak is observed in the transmittance spectrum for both Samples 1 and 2. In Fig. 2(a), all curves for $n_A \neq 0$ show that a single growing peak is located around $\lambda \approx 770$ nm for Sample 1. Clearly, as the groove number increases, the peak transmittance rises significantly. Therefore, this peak is confirmed as the single groove-generated peak. In addition to the single groove-generated peak, additional two peaks are observed for all curves for $n_A \neq 0$, one is located around $\lambda \approx 594$ nm and the other around $\lambda \approx 426$ nm. Meanwhile, the gray curve in Fig. 2(a), which is for the slit without grooves $(n_A = 0)$, also possesses two peaks, one is located at $\lambda \approx 620$ nm and the other at $\lambda \approx 448$ nm. Apparently, the locations of these two peaks are respectively close to the additional peaks (around $\lambda \approx 594$ nm and $\lambda \approx 426$ nm) of the curves

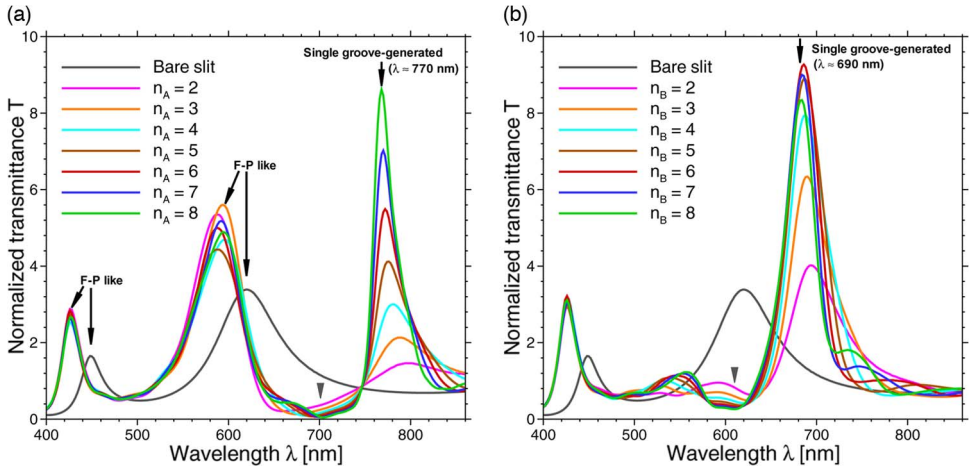

Fig. 2. Transmittance spectra (a) for different groove numbers, $2n_A$, for Sample 1 with $p_A = l_A = 730$ nm and (b) for different groove numbers, $2n_B$, for Sample 2 with $p_B = l_B = 600$ nm. In both (a) and (b), $w = 40$ nm, $h = 90$ nm, $a = 40$ nm, $t = 350$ nm, and $n_A = n_B = 2 \sim 8$.

for $n_A \neq 0$ in Fig. 2(a). Transmittances of the two additional peaks are not significantly affected by n_A. In fact, these two additional peaks (around $\lambda \approx 594$ nm and $\lambda \approx 426$ nm) are identified to associate with the F-P like resonance (i.e., slit resonance) for Sample 1. In other words, these two additional peaks are F-P like peaks. It is clear that the two F-P like peaks for the gray curve shift by about $22 \sim 26$ nm when the grooves are added on the bare slit. Similar phenomena for the F-P like peak shift could also be observed in the literature [26], [42]. Such shift could be due to the variation of the effective refractive index of the slit cavity when the surface corrugations are added to the metal film [42]. In short, the EOT of Sample 1 is characterized by the single groove-generated peak and two F-P like peaks.

In Fig. 2(b), similarly, a single peak is observed around $\lambda \approx 690$ nm for all curves for $n_B \neq 0$ for Sample 2. Also, as more grooves are added, the peak transmittance greatly rises. Therefore, this peak is confirmed to be the single groove-generated peak. A comparison between transmittance spectra for Samples 1 and 2, i.e., Fig. 2(a) and (b), shows that the wavelength of the single peak varies with the periodicity of the surrounding grooves. For example, as the groove periodicity is changed from a large pitch $p_A = 730$ nm to a relative small pitch $p_B = 600$ nm, the groove-generated peak wavelength varies from a long wavelength around $\lambda = 770$ nm [Fig. 2(a)] toward a relatively shorter wavelength around $\lambda = 690$ nm [Fig. 2(b)]. Obviously, this tendency of the wavelength shift implies that the groove-generated peak wavelength corresponds to the periodicity of the surrounding grooves. So far, the aforementioned spectral features for Samples 1 and 2, such as the occurrence of a single groove-generated EOT peak, are consistent with the previous report [26], even though the geometrical parameters used in this study are somewhat different from those used in the previous literature [26]. Briefly, Samples 1 and 2 show a single groove-generated peak in their transmittance spectra in Fig. 2(a) and (b), respectively, and the single peak for Samples 1 and 2 respectively occurs at the wavelength roughly equal to the groove period of the corresponding sample.

One thing that should be noted in Fig. 2 is that further addition of grooves does not add much to the transmittance. This is especially evident in Fig. 2(b) where addition of grooves 6–8 appears to result in no significant addition to the transmittance. This behavior could be attributed to the re-radiation (due to the corrugated surface) and the finite propagation length (due to the finite conductivity of real metals) of the SPP. The two phenomena limit the SPP collected by the surrounding grooves, especially when the grooves are far away from the slit. Therefore, adding many grooves to the surrounding arrays does not result in a linear increase in transmittance. In fact, such saturated results in transmittance in Fig. 2 are consistent with the transmission results for linear gratings reported in the literature [17].

In Fig. 2(a), one common F-P like peak around $\lambda \approx 594$ nm is observed for all the curves with $n_A \neq 0$. It is reasonable to think that this common F-P like peak should also be observed for all the curves with $n_B \neq 0$ since the transmittance curves for $n_B \neq 0$ and $n_A \neq 0$ are calculated for Sample 2 with the same film thickness which determines the transmittance features of F-P like peaks. However, in Fig. 2(b), we notice that the aforementioned common peak almost disappears [i.e., the peak transmittance is significantly lower compared with the one in Fig. 2(a)] around $\lambda \approx 594$ nm for all the curves with $n_B \neq 0$. The most likely explanation for the occurrence of the weak transmittance is that the Wood's anomaly offsets the intrinsic F-P like peak around $\lambda \approx 594$ nm in Fig. 2(b) for Sample 2. The Wood's anomaly comes from the onset of a new diffraction order that is tangential to the grating surface [43]. Note that the wavelength of the impinging light for the occurrence of the Wood's anomaly can be roughly predicted by the grating equation. The grating equation as below describes the relationship between the diffracted light and the impinging light:

$$\sin\theta_m = \sin\theta_i + \frac{m\lambda_w}{p}. \tag{3}$$

In (3), m is the diffracted order $(m = 0, \pm 1, \pm 2, \ldots)$, θ_m is the diffracted angle, θ_i is the incident angle of the impinging light, λ_w is the predicted wavelength for the occurrence of the Wood's anomaly, and p is periodicity of the grating.

The following demonstrates that the aforementioned nearly disappearing F-P like peak around $\lambda \approx 594$ nm in Fig. 2(b) is due to the Wood's anomaly. According to (3), the transmittance dip should occur at the calculated wavelength $\lambda_w = 600$ nm as $p = p_B = 600$ nm for the normal incidence, which corresponds to $\theta_i = 0^\circ$, $m = \pm 1$, and $\theta_m = \pm 90^\circ$ in (3). Evidently, the calculated wavelength $\lambda_w = 600$ nm is in a good agreement (a relative error of about $+1\%$) with the $\lambda \approx 594$ nm for the nearly disappearing F-P like peak in Fig. 2(b). That is, little light can pass the slit at the wavelength of λ_w such that a transmittance minimum appears. Similarly, a common dip (indicated by the gray inverted triangle) is observed around $\lambda \approx 700$ nm for all curves for $n_A \neq 0$ in Fig. 2(a) for Sample 1. This dip coincides with the wavelength $\lambda_w = 700$ nm calculated by (3) as well.

Up to now, the transmittance features of the spectra in Fig. 2(a) and (b) for Samples 1 and 2 are well analyzed, respectively. Next, we turn to investigate the spectral features of transmittance for Sample 3 and then make a comparison between spectral features for Sample 3 and those for Samples 1 and 2. Note that in the following subsections, Sample 3 is formed by combining the aforementioned Sample 1 with $n_A = 8$ and Sample 2 with $n_B = 6$ since the curve for $n_A = 8$ and the curve for $n_B = 6$ show the largest transmittance at its groove-generated EOT peak in Fig. 2(a) and (b), respectively.

3.2. Dual Groove-Generated EOT Peaks of Sample 3

The transmittance curve for Sample 3 with $n' \equiv (n_A; n_B) = (8; 6)$ is shown both in Fig. 3(a) and in Fig. 3(b). Interestingly, dual groove-generated EOT peaks are observed in this curve for Sample 3. The occurrence of the dual groove-generated EOT peaks could be confirmed by examining the transmittance spectra of Sample 3 with varying groove number n', as shown in Fig. 3(a) and (b). For instance, we fix $n_B = 6$ for Sample 2 and vary n_A (from 2 to 8) for Sample 1 and then combine Sample 1 with Sample 2 to form Sample 3 with varying $n' \equiv (n_A; n_B)$; the transmittance spectrum curves for Sample 3 are shown in Fig. 3(a). In Fig. 3(a), for the curves for $(n_A \neq 0; n_B = 6)$ for Sample 3, the first groove-generated EOT peak is observed around $\lambda \approx 790$ nm. This peak is confirmed as one of the dual groove-generated EOT peaks, since its peak transmittance is significantly growing with increasing n' (that is, n_A is increased from 2 to 8 for $(n_A; n_B)$ for Sample 3).

Similarly, we fix $n_A = 8$ for Sample 1 and vary n_B (from 2 to 6) for Sample 2 and combine Sample 1 with Sample 2 to form Sample 3 with varying $n' \equiv (n_A; n_B)$. The transmittance spectrum curves for Sample 3 are shown in Fig. 3(b). In Fig. 3(b), for the curves for $(n_A = 8; n_B \neq 0)$ for Sample 3, the second groove-generated EOT peak is observed around $\lambda \approx 690$ nm. This peak is confirmed as the other of the dual groove-generated EOT peaks, since its peak transmittance is significantly growing with increasing n' (that is, n_B is increased from 2 to 6 for $(n_A; n_B)$ for Sample 3).

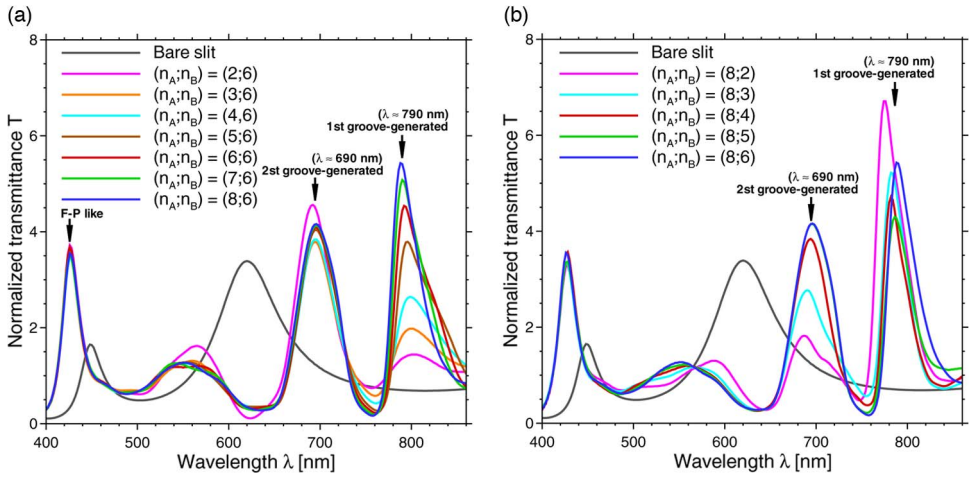

Fig. 3. Transmittance spectra for different groove numbers n' for Sample 3 which is formed by combining Samples 1 and 2. All geometrical parameters of Samples 1 and 2 are the same as in Fig. 2 except the groove numbers n_A and n_B. Here, the groove number n' is denoted by $(n_A; n_B)$ for (a) $n_A = 2 \sim 8$ and $n_B = 6$, and (b) $n_A = 8$ and $n_B = 2 \sim 6$.

Note that in Fig. 3(a) and (b), in addition to the dual groove-generated EOT peaks, an additional peak is observed at $\lambda \approx 426$ nm for all the transmittance curves for $(n_A \neq 0; n_B \neq 0)$ for Sample 3. This peak is confirmed as the F-P like peak for the following two reasons. First, the position and transmittance of this peak are almost not affected by the varying groove number n'. Second, the position of this peak is close to the position of the second F-P like peak of the gray curve (the case for bare slit).

As a result, from the transmittance curves for $(n_A \neq 0; n_B \neq 0)$ for Sample 3 in Fig. 3(a) and (b), it is seen that Sample 3 possesses dual groove-generated EOT peaks over the visible regime, unlike that each of Samples 1 and 2 possesses only a single one groove-generated peak over the same regime. It is worthy to note that the mixed-period grooves of Sample 3 are arranged with non-periodic groove pitches, unlike that the periodic grooves of Sample 1 or 2 are arranged with a constant groove pitch. On the other hand, not only periodic grooves but also non-periodic grooves can effectively assist optical transmission for a subwavelength slit, as long as the non-periodic groove pitches are carefully arranged like the mentioned Sample 3. Briefly, multiple EOT peaks such as the aforementioned dual groove-generated peaks are achieved via the proposed MPSG structure, namely Sample 3.

For comparison, the transmittance curve for Sample 3 with $n' \equiv (8; 6)$ and the curves for Sample 1 with $n_A = 8$ and Sample 2 with $n_B = 6$ are plotted in Fig. 4(a). In Fig. 4(a), the green and red dashed curves respectively show a single groove-generated peak located at $\lambda \approx 768$ nm (indicated by the green inverted triangle) and $\lambda \approx 686$ nm (indicated by the red inverted triangle) for Samples 1 and 2; the blue solid curve shows dual groove-generated peaks (indicated by the blue inverted triangles) located at $\lambda \approx 788$ nm (indicated by the 1st blue inverted triangle) and $\lambda \approx 696$ nm (indicated by the 2nd blue inverted triangle) for Sample 3. From Fig. 4(a), it can be seen that the positions of the first and second groove-generated EOT peaks for Sample 3 have strong correspondences with the relative positions of the single groove-generated EOT peaks of Samples 1 and 2. For example, the wavelength of the first peak (at $\lambda \approx 788$ nm) for Sample 3 is close to that of the single peak (at $\lambda \approx 768$ nm) for Sample 1, and the wavelength of the second peak (at $\lambda \approx 696$ nm) for Sample 3 is close to that of the single peak $(\lambda \approx 686$ nm$)$ for Sample 2. Hence, based on the similarities for groove-generated peak wavelengths between Sample 3 and Samples 1 and 2, we believe that the occurrence of the dual groove-generated peaks is associated with particular implicit groove periodicities which are hidden in the mixed-period grooves of Sample 3. Furthermore, it is clear from Fig. 4(a) that such implicit groove periodicities may come from the groove periodicities of surrounding periodic grooves of Samples 1 and 2, that is, $p_A = 730$ nm and $p_B = 600$ nm, respectively.

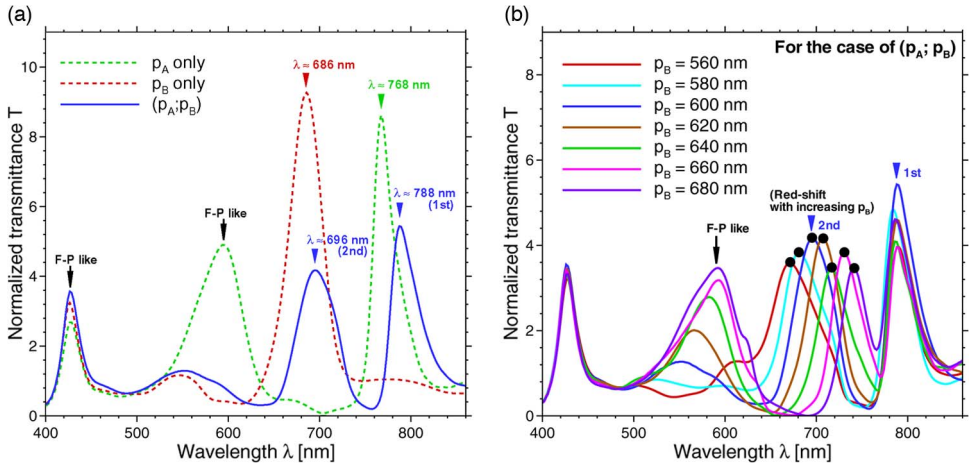

Fig. 4. (a) Comparison of transmittance curves between groove-generated EOT peaks for the same Sample 3 [with $n' \equiv (8;6)$] in Fig. 3 and those of the same Samples 1 (with $n_A = 8$) and 2 (with $n_B = 6$) in Fig. 2. Here, the cases for Samples 1, 2, and 3 are denoted by green dashed, red dashed, and blue solid curves, respectively. (b) Transmittance curves for different p_B for the same Sample 3 in (a), where p_B ranges from 560 nm to 680 nm. In (b), the black solid circle indicates the second groove-generated peak of each curve.

In order to understand more about the mixed-period grooves of Sample 3, we combine Sample 1 with a fixed groove period and Sample 2 with a varying groove period to form Sample 3 for checking the relation between the groove-generated peaks and the mixed-period grooves. As an example, the transmittance spectra in Fig. 4(b) show the dependences of the groove-generated peaks for different p_B's for the same Sample 3 in Fig. 4(a). Here, p_B ranges from 560 nm to 680 nm with a step size of 20 nm. Two spectra features for the groove-generated peaks can be observed from the curves in Fig. 4(b). First, the first groove-generated peak of Sample 3 appears at almost the same position. This indicates that the peak wavelength of the first-groove generated peak is only dependent on p_A and not affected by p_B. Second, when p_B increases, the second groove-generated peak red-shifts with a step size of about 10 nm. Based on the two results, one may conclude that the groove-generated peak of Sample 3 can be tuned by changing the groove pitches of the mixed-period grooves. By the way, Fig. 4(b) shows noticeable transmittance peaks around $\lambda \approx 594$ nm for the curves for $p_B > 620$ nm, which are the F-P like peaks. These F-P like peaks arise again due to the red-shift of the wavelength of the aforementioned Wood's anomaly.

3.3. Mechanism of Dual Groove-Generated EOT Peaks

It is interesting that the MPSG structure (that is, the aforementioned Sample 3) with irregular groove pitches possesses dual groove-generated EOT peaks, as revealed in the blue solid transmittance curve in Fig. 4(a). In order to identify the mechanism of the dual groove-generated EOT peaks, amplitudes of the magnetic field $(\mathrm{Re}[H_z])$ associated with the groove-generated peaks at $\lambda = 788$ nm and $\lambda = 696$ nm of the blue solid curve are plotted in the left panels of Fig. 5(a) and (b), respectively.

As is shown in the left panel of Fig. 5(a), the SPP is clearly evident on the exit surface (i.e., the metal-dielectric interface at $x = 350$ nm) of Sample 3. For comparison, the field for the bare slit (that is, removing all the grooves of Sample 3) at $\lambda = 788$ nm [the first groove-generated peak in Fig. 4(a)] is plotted in the right panel in Fig. 5(a). It is shown that the SPP coming from the subwavelength slit is not clearly evident on the exit surface of the bare slit because the coupling of energy between light and SPP is low for the subwavelength slit. Consequently, it is reasonable to deduce that the significant SPP on the exit surface of Sample 3 in the left panel of Fig. 5(a) is caused by the mixed-period grooves. Similarly, from comparing the left panel with the right panel in Fig. 5(b), it is clear that Sample 3 allows more SPPs to pass through the subwavelength slit when

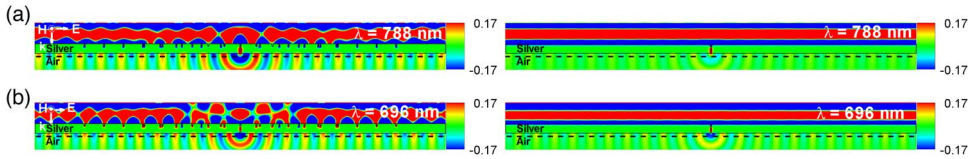

Fig. 5. Distributions of magnetic field, Re$[H_z]$, for the same Sample 3 in Fig. 4(a) and the corresponding bare slit. In (a) and (b), the field distributions (left panels for Sample 3 and right panels for the bare slit) are associated with $\lambda = 788$ nm and $\lambda = 696$ nm, respectively. The dashed curve below the metal film denotes the position near the exit surface, namely $x = 352.5$ nm. Length spans on each panel: $x = 1.76$ μm, $y = 15.39$ μm. The color bar limits are set to ± 0.17 ampere per meter.

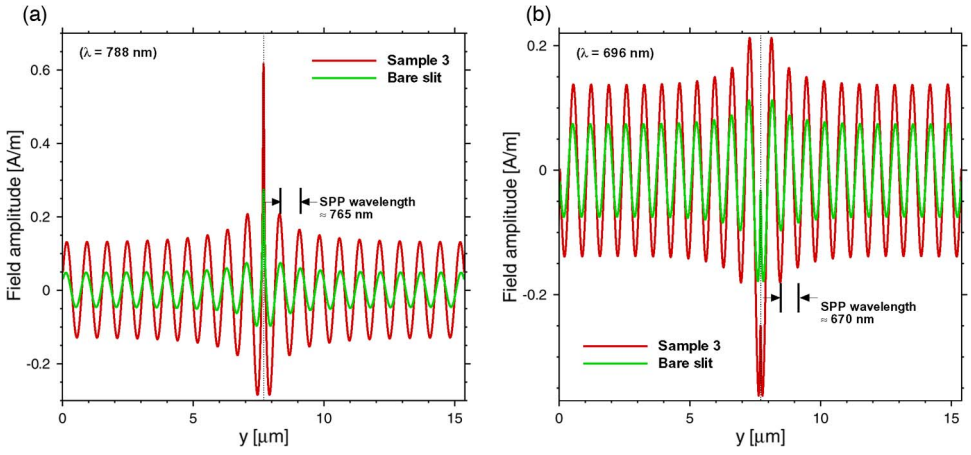

Fig. 6. The magnetic-field magnitudes (Re$[H_z]$), of the surface waves near the exit surface along the horizontal line at $x = 352.5$ nm (the dash lines in Fig. 5) for (a) the structure in Fig. 5(a) and (b) the structure in Fig. 5(b). The red curves are for Sample 3 and the green curves are for the bare slit. The vertical dotted lines denote the centerline of the slit, namely $y = 7.695$ μm.

$\lambda = 696$ nm [the second groove-generated peak in Fig. 4(a)]. Accordingly, we conclude that the dual groove-generated EOT peaks of the blue curve in Fig. 4(a) are directly related to the SPPs launched by the mixed-period grooves. To be specific, at the dual incident wavelengths (i.e., $\lambda = 788$ nm and $\lambda = 696$ nm), the excited groove-generated SPPs and the excited slit-generated SPPs carry the incident energy to propagate along the slit wall to pass through the slit exit, thus leading to the dual groove-generated EOT peaks in the transmittance spectrum for Sample 3.

We also checked the wavelength of the SPP launched by the mixed-period grooves and the slit. The SPP wavelength is usually estimated using the following expression [44]:

$$\lambda_{\mathrm{SPP}} = \mathrm{Re}\left(\lambda\sqrt{\frac{\varepsilon_{\mathrm{d}} + \varepsilon_{\mathrm{m}}}{\varepsilon_{\mathrm{d}} \cdot \varepsilon_{\mathrm{m}}}}\right). \tag{4}$$

In (4), λ and ε_{d} are the incident wavelength in free space and the relative permittivity of the dielectric, respectively. Note that λ_{SPP} is usually smaller than λ. Thus, via (4), we know that the SPP wavelengths in Fig. 5(a) and (b) are $\lambda_{\mathrm{SPP}}^{(1\mathrm{st})} \approx 773.7$ nm, corresponding to the first groove-generated EOT peak at $\lambda = 788$ nm, and $\lambda_{\mathrm{SPP}}^{(2\mathrm{nd})} \approx 678.9$ nm, corresponding to the second groove-generated EOT peak at $\lambda = 696$ nm, respectively. Fig. 6(a) and (b) plot the magnetic-field amplitudes (Re$[H_z]$) of the surface wave on the exit surface for Sample 3 and the bare slit in Fig. 5(a) and (b), respectively. It is clear from Fig. 6(a) and (b) that SPP wavelengths near the exit surface along the horizontal line at $x = 352.5$ nm calculated from the FDTD method are 765 nm and 670 nm, respectively. Evidently, The SPP wavelengths calculated from our numerical simulations are smaller but very close to those obtained from Eq. (4). Therefore, it is confirmed that Sample 3 makes the

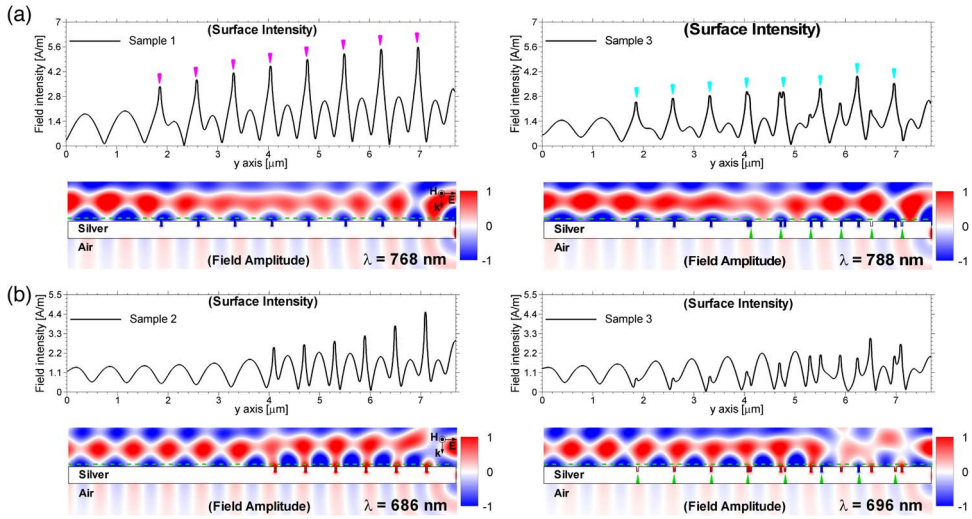

Fig. 7. Distributions of magnetic field (the color contour), Re$[H_z]$, for the same Sample 3 and the same Samples 1 and 2 in Fig. 4(a). In (a), left panel (for Sample 1) is associated with $\lambda = 768$ nm and right panel (for Sample 3) is associated with $\lambda = 788$ nm. In (b), left panel (for Sample 2) is associated with $\lambda = 686$ nm and right panel (for Sample 3) is associated with $\lambda = 696$ nm. The black curves show the intensity of magnetic field on the horizontal line with $x = -2.5$ nm (indicated by the green dashed lines) above the grooves, which is the surface field intensity, $|H_z|$, for the SPPs. For simplicity, each panel shows only the left half-diagram for the symmetrical field distribution. The color bar limits are set to ± 1 ampere per meter.

dual groove-generated EOT peaks by the mixed-period grooves via the excitation of the SPP. In addition, the comparison between the green and red curves in Fig. 6(a) and in (b) shows that the SPPs generated by the mixed-period grooves and those generated by the single bare slit have the same SPP wavelength. This is because the SPP wavelength depends only on the incident wavelength and the material, not on the geometry of the structure. Here, the mixed-period grooves act like a combined grating coupler which converts the incident light into the SPP at multiple incident wavelengths. This characteristic makes the MPSG structure have potential applications in photonic devices with multiple operating wavelengths.

By the way, we noticed that in Fig. 4(a), the transmittances of the dual groove-generated EOT peaks at $\lambda = 788$ nm and $\lambda = 696$ nm for Sample 3 (the blue solid cure) are smaller than those of the single groove-generated EOT peak at $\lambda = 768$ nm for Sample 1 (the green dashed cure) and the single groove-generated EOT peak at $\lambda = 686$ nm for Sample 2 (the red dashed cure), respectively. Such difference in transmittance of groove-generated peaks between Sample 3 and Samples 1 and 2 can be understood from the magnetic field intensity of the surface waves near the input surface of the corresponding sample. For example, the surface field intensity (black curve) in the left panel in Fig. 7(a) shows that the grooves arranged with $p_A = 730$ nm on the left side of the slit of Sample 1 have strong field intensities above the grooves' openings, with most peak intensities being larger than 3.92 A/m indicated by the pink inverted triangles. In contrast, the surface field intensity (black curve) in the right panel in Fig. 7(a) shows that the grooves arranged with the groove pitch of $p_A = 730$ nm on the left side of the slit of Sample 3 have weaker field intensities above the grooves' openings, with all peak intensities being lower than 3.92 A/m indicated by the cyan inverted triangles. Similarly, such difference in surface field intensity is also observed between Samples 2 and 3. That is, the field above the grooves with $p_B = 600$ nm on the left side of the slit of Sample 2 have stronger surface intensities than the ones among the mixed-period grooves of Sample 3, as shown by the black curves in the left and right panels in Fig. 7(b), respectively. Therefore, from the left and right panels in Fig. 7, it can be seen that Sample 3 has weaker surface field intensities than Samples 1 and 2. Such difference in the surface field intensity between Sample 3 and Samples 1 and 2 in Fig. 7 might be attributed to the fact that Sample 3 has more surface

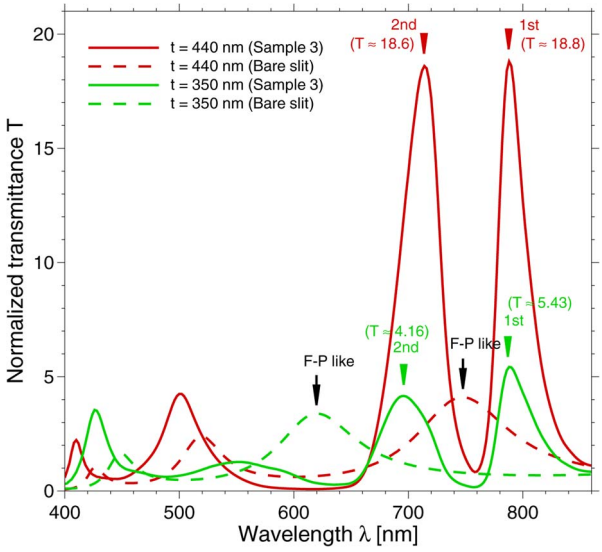

Fig. 8. Transmittance spectra for Sample 3 with different film thicknesses t. For each solid transmittance curve, all geometrical features and parameters of Sample 3 are the same as those of Sample 3 in Fig. 4(a) except for the film thickness $t = 440$ nm for the red solid curve. The red and the green dashed transmittance curves, respectively, are for the bare slit associated with the same Sample 3 for the red and green solid curves.

grooves than Sample 1 (Sample 2) such that the surface waves of Sample 3 suffer more propagation losses due to the scattering effect when surface waves hit the surface grooves.

In order to boost the transmittances of the dual groove-generated peaks for Sample 3, one way is given here. That is, to vary the film thickness. Fig. 8 shows the transmittance spectra for Sample 3 for two different film thicknesses. With an appropriate film thickness, it is obvious from the red and green solid curves in Fig. 8 that the transmittances of the dual groove-generated peaks can be simultaneously promoted. For example, in the green solid curve for Sample 3 with $t = 350$ nm in Fig. 8, the transmittances of the first (at $\lambda = 788$ nm, indicated by the first green inverted triangle) and second (at $\lambda = 696$ nm, indicated by the second green inverted triangle) groove-generated peaks are $T \approx 5.43$ and $T \approx 4.16$, respectively, while in the red solid curve for Sample 3 with $t = 440$ nm in the same figure, the first (at $\lambda = 788$ nm, indicated by the first red inverted triangle) and second (at $\lambda = 714$ nm, indicated by the second red inverted triangle) groove-generated peaks are raised to $T \approx 18.8$ and $T \approx 18.6$, respectively. The transmittance enhancements are 3.5 and 4.5 times, respectively.

The aforementioned transmittance promotion can be understood by comparing the transmittance curves for Sample 3 with $t = 440$ nm and $t = 350$ nm with those for the bare slits associated with the corresponding thicknesses. The red dashed curve for the bare slit with $t = 440$ nm shows that the first F-P like peak at $\lambda \approx 748$ nm (indicated by the black inverted triangle) has a broad line shape, which basically overlaps with the wavelength ranges (roughly from $\lambda \approx 680$ nm to 830 nm) associated with the dual groove-generated peaks (indicated by the red inverted triangles) for the red solid curve for Sample 3 with $t = 440$ nm. In contrast, the green dashed curve for the bare slit with $t = 350$ nm in Fig. 8 indicates that the first F-P like peak at $\lambda \approx 620$ nm (indicated by the black inverted triangle) has a broad line shape (roughly from $\lambda \approx 580$ nm to 660 nm), which does not overlap with the wavelength ranges (roughly from $\lambda \approx 680$ nm to 830 nm) associated with the dual groove-generated peaks (indicated by the green inverted triangles) for the green solid curve for Sample 3 with $t = 350$ nm. Accordingly, it is confirmed that the transmittance promotion for the dual groove-generated EOT peaks in Fig. 8 is directly related to the position of the F-P like resonance of the subwavelength slit. As a result, we conclude that with an appropriate film thickness, the F-P like resonance of the subwavelength slit can be utilized to boost the multiple groove-generated peaks of the MPSG structure.

4. Conclusion

In summary, we have proposed a design for 1-D non-periodic grooves, namely the mixed-period grooves, to surround a subwavelength slit to achieve multiple groove-generated EOT peaks. In fact, the proposed MPSG structure is formed by combining two SPSG structures mainly with different groove periodicities. Based on the transmittance spectra calculated by the FDTD method, our simulation results suggest that the MPSG structure with the mixed-period grooves can possess dual groove-generated EOT peaks. Moreover, this work has numerically shown that the dual groove-generated peaks are due to the excitation of the SPPs via the mixed-period grooves. Furthermore, we have demonstrated that the dual groove-generated EOT peaks of the MPSG structure can be further enhanced by fine-tuning the film thickness. We believe that our finding can be helpful for expanding the number of the operating wavelengths in the visible regime for some plasmonic devices.

References

[1] H. A. Bethe, "Theory of diffraction by small holes," *Phys. Rev.*, vol. 66, no. 7/8, pp. 163–182, Oct. 1944.
[2] E. Ozbay, "Plasmonics: Merging photonics and electronics at nanoscale dimensions," *Science*, vol. 311, no. 5758, pp. 189–193, Jan. 2006.
[3] T. W. Ebbesen, H. J. Lezec, H. F. Ghaemi, T. Thio, and P. A. Wolff, "Extraordinary optical transmission through sub-wavelength hole arrays," *Nature*, vol. 391, no. 6668, pp. 667–669, Feb. 1998.
[4] Y. Xie, A. Zakharian, J. Moloney, and M. Mansuripur, "Transmission of light through slit apertures in metallic films," *Opt. Exp.*, vol. 12, no. 25, pp. 6106–6121, Dec. 2004.
[5] N. Rotenberg, M. Spasenovi, T. L. Krijger, B. L. Feber, F. J. Garcia de Abajo, and L. Kuipers, "Plasmon scattering from single subwavelength holes," *Phys. Rev. Lett.*, vol. 108, no. 12, pp. 127402-1–127402-5, Mar. 2012.
[6] H. Liu and P. Lalanne, "Microscopic theory of the extraordinary optical transmission," *Nature*, vol. 452, no. 7188, pp. 728–731, Apr. 2008.
[7] S. H. Chang, S. Gray, and G. Schatz, "Surface plasmon generation and light transmission by isolated nanoholes and arrays of nanoholes in thin metal films," *Opt. Exp.*, vol. 13, no. 8, pp. 3150–3165, Apr. 2005.
[8] J. Porto, F. J. Garcia-Vídal, and J. Pendry, "Transmission resonances on metallic gratings with very narrow slits," *Phys. Rev. Lett.*, vol. 83, no. 14, pp. 2845–2848, Oct. 1999.
[9] C. Genet and T. W. Ebbesen, "Light in tiny holes," *Nature*, vol. 445, no. 7123, pp. 39–46, Jan. 2007.
[10] M. Consonni, J. Hazart, and G. Lérondel, "Fabry–Pérot-type enhancement in plasmonic visible nanosource," *Appl. Phys. Lett.*, vol. 94, no. 5, pp. 051105-1–051105-3, Feb. 2009.
[11] W. Srituravanich, N. Fang, C. Sun, Q. Luo, and X. Zhang, "Plasmonic nanolithography," *Nano lett.*, vol. 4, no. 6, pp. 1085–1088, Jun. 2004.
[12] G. Gbur, H. F. Schouten, and T. D. Visser, "Achieving superresolution in near-field optical data readout systems using surface plasmons," *Appl. Phys. Lett.*, vol. 87, no. 19, pp. 191109-1–191109-3, Nov. 2005.
[13] C. Liu, V. Kamaev, and Z. V. Vardeny, "Efficiency enhancement of an organic light-emitting diode with a cathode forming two-dimensional periodic hole array," *Appl. Phys. Lett.*, vol. 86, pp. 143501-1–143501-1, Apr. 2005.
[14] T. Ishi, J. Fujikata, K. Makita, T. Baba, and K. Ohashi, "Si nano-photodiode with a surface plasmon antenna," *Jpn. J. Appl. Phys.*, vol. 44, no. 12, pp. L364–L366, Mar. 2005.
[15] Z. Yu, G. Veronis, S. Fan, and M. L. Brongersma, "Design of midinfrared photodetectors enhanced by surface plasmons on grating structures," *Appl. Phys. Lett.*, vol. 89, no. 115, pp. 151116-1–151116-3, Oct. 2006.
[16] L. A. Dunbar, M. Guillaumée, F. de León-Pérez, C. Santschi, E. Grenet, R. Eckert, F. Lopez-Tejeira, F. J. García-Vidal, L. Martín-Moreno, and R. P. Stanley, "Enhanced transmission from a single subwavelength slit aperture surrounded by grooves on a standard detector," *Appl. Phys. Lett.*, vol. 95, no. 1, pp. 011113-1–011113-3, Jul. 2009.
[17] R. D. R. Bhat, N. C. Panoiu, S. R. J. Brueck, and R. M. Osgood, "Enhancing the signal-to-noise ratio of an infrared photodetector with a circular metal grating," *Opt. Exp.*, vol. 16, no. 7, pp. 4588–4596, Mar. 2008.
[18] T. Thio, K. M. Pellerin, R. A. Linke, H. J. Lezec, and T. W. Ebbesen, "Enhanced light transmission through a single subwavelength aperture," *Opt. Lett.*, vol. 26, no. 24, pp. 1972–1974, Dec. 2001.
[19] H. J. Lezec, A. Degiron, E. Devaux, R. Linke, L. Martin-Moreno, F. J. García-Vidal, and T. W. Ebbesen, "Beaming light from a subwavelength aperture," *Science*, vol. 297, no. 5582, pp. 820–822, Aug. 2002.
[20] S. Carretero-Palacios, O. Mahboub, F. J. García-Vidal, L. Martin-Moreno, S. G. Rodrigo, C. Genet, and T. W. Ebbesen, "Mechanisms for extraordinary optical transmission through bull's eye structures," *Opt. Exp.*, vol. 19, no. 11, pp. 10 429–10 442, May 2011.
[21] O. Mahboub, S. C. Palacios, C. Genet, F. J. García-Vidal, S. G. Rodrigo, L. Martin-Moreno, and T. W. Ebbesen, "Optimization of bull's eye structures for transmission enhancement," *Opt. Exp.*, vol. 18, no. 11, pp. 11 292–11 299, May 2010.
[22] T. Thio, H. J. Lezec, T. W. Ebbesen, K. M. Pellerin, G. D. Lewen, A. Nahata, and R. A. Linke, "Giant optical transmission of sub-wavelength apertures: Physics and applications," *Nanotechnology*, vol. 13, no. 3, pp. 429–432, Jun. 2002.
[23] A. Degiron and T. W. Ebbesen, "Analysis of the transmission process through single apertures surrounded by periodic corrugations," *Opt. Exp.*, vol. 12, no. 16, pp. 3694–3700, Aug. 2004.

[24] C. Chen, N. Verellen, K. Lodewijks, L. Lagae, G. Maes, G. Borghs, and P. Van Dorpe, "Groove-gratings to optimize the electric field enhancement in a plasmonic nanoslit-cavity," *J. Appl. Phys.*, vol. 108, no. 3, pp. 034319-1–034319-8, Aug. 2010.
[25] L. L. Wang, X. F. Ren, R. Yang, G. C. Guo, and G. P. Guo, "Transmission of doughnut light through a bull's eye structure," *Appl. Phys. Lett.*, vol. 95, no. 11, pp. 111111-1–111111-3, Sep. 2009.
[26] F. J. García-Vidal, H. J. Lezec, T. W. Ebbesen, and L. Martín-Moreno, "Multiple paths to enhance optical transmission through a single subwavelength slit," *Phys. Rev. Lett.*, vol. 90, no. 21, pp. 213901-1–213901-4, May 2003.
[27] L. Cai, G. Li, F. Xiao, Z. Wang, and A. Xu, "Theory of enhanced optical transmission through a metallic nano-slit surrounded with asymmetric grooves under oblique incidence," *Opt. Exp.*, vol. 18, no. 19, pp. 19 495–19 503, Sep. 2010.
[28] Z. B. Li, Y. H. Yang, X. T. Kong, W. Y. Zhou, and J. G. Tian, "Fabry–Pèrot resonance in slit and grooves to enhance the transmission through a single subwavelength slit," *J. Opt. A, Pure Appl. Opt.*, vol. 11, no. 10, pp. 105002-1–105002-4, Oct. 2009.
[29] L. Cai, G. Li, Z. Wang, and A. Xu, "Interference and horizontal Fabry–Pèrot resonance on extraordinary transmission through a metallic nanoslit surrounded by grooves," *Opt. Lett.*, vol. 35, no. 2, pp. 127–129, Jan. 2010.
[30] C. K. Chang, D. Z. Lin, C. S. Yeh, C. K. Lee, Y. C. Chang, M. W. Lin, J. T. Yeh, and J. M. Liu, "Similarities and differences for light-induced surface plasmons in one- and two-dimensional symmetrical metallic nanostructures," *Opt. Lett.*, vol. 31, no. 15, pp. 2341–2343, Aug. 2006.
[31] A. Agrawal, H. Cao, and A. Nahata, "Time-domain analysis of enhanced transmission through a single subwavelength aperture," *Opt. Exp.*, vol. 13, no. 9, pp. 3535–3542, May 2005.
[32] D. A. Thomas and H. P. Hughes, "Enhanced optical transmission through a subwavelength 1D aperture," *Solid State Commun.*, vol. 129, no. 8, pp. 519–524, Feb. 2004.
[33] C. M. Wang, H. I. Huang, C. C. Chao, J. Y. Chang, and Y. Sheng, "Transmission enhancement through a trench-surrounded nano metallic slit by bump reflectors," *Opt. Exp.*, vol. 15, no. 6, pp. 3496–3501, Mar. 2007.
[34] Y. X. Cui, S. He, and Y. Okuno, "Giant optical transmission through a metallic nano-slit achieved by the optimization of the groove periodicity and other parameters," in *Proc. Int. Workshop Metamater.*, Nanjing, China, Nov. 2008, pp. 236–239.
[35] O. T. A. Janssen, H. P. Urbach, and G. W. t Hooft, "Giant optical transmission of a subwavelength slit optimized using the magnetic field phase," *Phys. Rev. Lett.*, vol. 99, no. 4, pp. 43902-1–43902-4, Jul. 2007.
[36] P. Lalanne and J. P. Hugonin, "Interaction between optical nano-objects at metallo-dielectric interfaces," *Nat. Phys.*, vol. 2, no. 8, pp. 551–556, Aug. 2006.
[37] F. J. Garcìa-Vidal, L. Martin-Moreno, T. W. Ebbesen, and L. Kuipers, "Light passing through subwavelength apertures," *Rev. Mod. Phys.*, vol. 82, no. 1, pp. 729–787, Mar. 2010.
[38] H. J. Lezec and T. Thio, "Diffracted evanescent wave model for enhanced and suppressed optical transmission through subwavelength hole arrays," *Opt. Exp.*, vol. 12, no. 16, pp. 3629–3651, Aug. 2004.
[39] Y. Cui and S. He, "A theoretical re-examination of giant transmission of light through a metallic nano-slit surrounded with periodic grooves," *Opt. Exp.*, vol. 17, no. 16, pp. 13 995–14 000, Aug. 2009.
[40] A. Taflove and S. C. Hagness, *Computational Electrodynamics: The Finite-Difference Time-Domain Method*, 3rd ed. Norwood, MA, USA: Artech House, 2005.
[41] D. W. Lynch and W. R. Hunter, "SILVER (Ag)," in *Handbook of Optical Constants of Solids*, E. D. Palik, Ed. New York, NY, USA: Academic Press, 1985, pp. 350–357.
[42] V. Marrocco, R. Marani, M. Grande, G. Morea, G. Calò, V. Petruzzelli, and A. D'Orazio, "Modification of the scattering of silver nanoparticles induced by Fabry-Pérot resonances rising from a finite Si layer," *J. Opt.*, vol. 13, no. 1, pp. 015004-1–015004-9, Jan. 2011.
[43] A. Hessel and A. A. Oliner, "A new theory of Wood's anomalies on optical gratings," *Appl. Opt.*, vol. 4, no. 10, pp. 1275–1297, Oct. 1965.
[44] H. Raether, *Surface Plasmons on Smooth and Rough Surfaces and on Gratings*, 1st ed. New York, NY, USA: Springer-Verlag, 2005, p. 5.